buildings

MDPI

Article

Dynamic Characteristics of Geogrid-Reinforced Foamed Lightweight Soil Under Cyclic Loading

Yong Liu [1], Yinhe Li [2,*] and Yuan Sun [3]

[1] School of Transportation and Civil Engineering, Shandong Jiaotong University, Jinan 250357, China; 204042@sdjtu.edu.cn
[2] The College of Architecture and Civil Engineering, Beijing University of Technology, Beijing 100124, China
[3] School of Architecture and Planning, Yunnan University, Kunming 650500, China; 20241150036@stu.ynu.edu.cn
* Correspondence: liyinhe@emails.bjut.edu.cn

Abstract

Although foamed lightweight soil is widely used for its light weight and high strength, its insufficient dynamic performance under cyclic loading and the poorly understood reinforcement mechanism have become key bottlenecks restricting its optimized application. To investigate the dynamic characteristics and influencing factors of geogrid-reinforced foamed lightweight soil (GRFLS), laboratory dynamic triaxial tests were conducted using a DJSZ-100D dynamic–static triaxial testing system. The effects of the number of geogrid layers and wet density on the dynamic mechanical properties were examined, with analysis focused on failure patterns, backbone curves, dynamic strength, dynamic shear modulus, and damping ratio. The results indicate that the inclusion of geogrids effectively restrained the propagation of longitudinal cracks in the foamed lightweight soil. The hyperbolic backbone curves were well characterized by the Hardin–Drnevich model. An increase in wet density significantly enhanced the dynamic strength, and an optimal number of two reinforcement layers was identified based on the reinforced strength–stress ratio. The dynamic elastic modulus and damping ratio of GRFLS increased with growing dynamic strain. Compared with the unreinforced condition, the initial dynamic elastic modulus of the specimens with two geogrid layers increased by an average of 15.6%, and the maximum damping ratio increased by an average of 12.9%. While both geogrid reinforcement and higher wet density effectively increased the dynamic elastic modulus, only an increase in wet density notably improved the damping ratio. Finally, predictive models for the enhanced dynamic elastic modulus and damping ratio, which incorporate wet density and the number of reinforcement layers, were established. These models indirectly reflect the dynamic deviator stress–strain relationship of GRFLS. This study provides a theoretical basis for engineering construction.

Keywords: foamed lightweight soil; geogrid reinforcement; multi-stage cyclic loading; dynamic mechanical properties; dynamic triaxial test; dynamic elastic modulus; damping ratio; calculation model

Check for updates

Academic Editor: Cedric Payan

Received: 8 May 2026
Revised: 11 June 2026
Accepted: 15 June 2026
Published: 18 June 2026

Copyright: © 2026 by the authors. Licensee MDPI, Basel, Switzerland. This article is an open access article distributed under the terms and conditions of the Creative Commons Attribution (CC BY) license.

1. Introduction

Foamed lightweight soil (FLS) is a lightweight material containing a large number of closed air pores, produced by mixing cement, water, and a foaming agent in specific proportions, followed by hardening through physical and chemical reactions [1]. It offers advantages such as high fluidity, controllable mechanical properties, light weight combined

with high strength, thermal insulation, fire resistance, sound insulation, seismic resistance, and durability [2]. Consequently, FLS has been widely used in various geotechnical engineering applications [3,4], particularly in highway subgrade replacement for load reduction [5], tunnel seismic isolation [6], backfill behind abutments [7], high-speed railway embankment construction [8,9], railway subgrade widening [10], and structural vibration isolation [11]. However, FLS in these applications is inevitably subjected to dynamic loads from traffic, waves, earthquakes, and other sources, making the consideration of vibrational load effects essential.

Conventional compacted fill typically has a density ranging from 1800 to 2100 kg/m^3 [12], resulting in large vertical additional stresses. When placed on problematic foundations such as existing and new subgrades [13] or soft soils [14], it can easily induce excessive post-construction settlement, differential settlement, and even foundation instability. To address this issue, extensive research has been conducted on lightweight fill materials, including foamed lightweight soil [15,16], EPS [17], ceramsite concrete [18], and tire shred–soil mixtures [19]. Shi et al. [20] investigated the dynamic mechanical behavior, energy absorption, and damage characteristics of ceramsite-based foamed concrete, finding that the peak stress and energy absorption density increased by 151% and 211%, respectively. Hao et al. [11] studied the natural vibration period, damping ratio, and seismic response of a novel prefabricated fly ash foamed concrete structure, reporting that the effect of damping on the natural period and mode shape was within 9.0%, with a structural damping ratio of 0.059, and proposed a damping-considered period calculation method. Wen et al. [21] reported a damping ratio of 0.366 for saponification residue-fly ash foamed lightweight soil with a dry density of 400 kg/m^3. Furthermore, extensive research has demonstrated that the porous structure of FLS enhances its strength by reducing pore volume and promoting crack formation, thereby endowing it with favorable damping characteristics and robust dynamic stability [22]. When used as subgrade backfill, the failure mode of FLS transitions gradually from tensile failure to shear failure as its thickness increases. Consequently, enhancing its dynamic performance through material modification or structural reinforcement has become a key research focus in the field of engineering materials.

Existing research has predominantly focused on the behavior of FLS under static loading conditions [23–25]. However, as engineering structures are frequently subjected to dynamic loads in practice, findings from static load studies are often insufficient to meet actual engineering demands. In response, scholars have conducted a series of investigations into the dynamic characteristics of FLS [26,27]. Its dynamic properties exhibit significant density dependence, with the critical dynamic stress increasing as density rises [28]. The dynamic stress–strain curves of FLS show notable fluctuations: low-density specimens absorb energy primarily through pore compaction, whereas high-density specimens absorb energy through the propagation of internal microcracks [22]. Wu et al. [29] found that silt-based foamed lightweight soil exhibits typical elastoplastic characteristics, with dynamic strength increasing with wet density but decreasing with higher silt content. They also developed a quantitative model based on the Ramberg–Osgood equation relating damage variables to plastic strain and number of cycles. Li et al. [30] and Gong et al. [31] employed a Split Hopkinson Pressure Bar (SHPB) system to study the dynamic properties of FLS under impact loading, revealing that its dynamic mechanical performance improves with increasing strain rate, indicating excellent energy absorption capacity [32]. According to Mu et al. [26], long-term cyclic loading tests on FLS show that static compressive strength peaks and then drops as the initial dynamic load amplitude grows. Concurrently, cumulative strain accumulates with dynamic stress and cycle number, leading ultimately to brittle failure [29]. It was found that the dynamic shear modulus of foamed lightweight soil increases with greater dynamic strain [33], confining pressure [34], and wet density [35];

however, it demonstrates an initial increase followed by a decrease as the number of loading cycles rises. In contrast, the damping ratio first decreases and then increases with increasing dynamic strain.

Currently, research on composite FLS primarily focuses on the utilization of solid waste materials [36], the investigation and development of mix proportions [37], and the fundamental mechanical properties alongside their underlying micromechanisms [38]. Conventional FLS is prone to tensile and shear failures, yet there is a notable lack of studies on its reinforcement through material treatment and structural modification using geosynthetics. Although significant research has been conducted on fiber-reinforced [39,40] and steel bar-reinforced foamed lightweight soil [41,42], detailed investigations into GRFLS remain scarce. This gap is insufficient to address the complex conditions and scenarios encountered in practical subgrade engineering applications, thereby limiting its broader engineering adoption. As a novel, eco-friendly construction material [43], GRFLS holds promising application prospects in the field of road engineering. However, a comprehensive and systematic evaluation of its dynamic mechanical performance has not yet been performed. Thus, further research into its dynamic characteristics is necessary to guide the practical application of this material.

GRFLS is an innovative geotechnical composite material whose mechanism of action differs significantly from that of ordinary FLS. Although some studies have investigated the dynamic properties of FLS, the effects of the number of reinforcement layers and wet density on the dynamic elastic modulus and damping ratio of GRFLS under cyclic loading remain poorly understood, and relevant research is still lacking. This knowledge gap is particularly critical when the material is used as fill, as the evolution of its mechanical properties under cyclic loading cannot be overlooked. Therefore, this paper systematically investigates the failure mode, backbone curve, dynamic strength, dynamic elastic modulus, and damping ratio of GRFLS through graded cyclic loading dynamic triaxial tests. The objective is to reveal the influence mechanisms of reinforcement layers and wet density on its dynamic characteristics, and to establish a strengthening model for the dynamic elastic modulus and a prediction model for the damping ratio, thereby providing a theoretical basis for its practical engineering applications.

2. Materials and Methods

2.1. Materials

The experiment utilized a bi-directional plastic geogrid [44], selected for its high tensile strength and low cost. The geogrid, manufactured from polypropylene (PP), was cut into circular disks with a diameter of 145 mm [45] and an individual aperture size of 33 mm × 33 mm, as shown in Figure 1. The key performance parameters of the geogrid are listed in Table 1. Ordinary Portland Cement (P·O 42.5 grade) was employed, and its physical and mechanical properties are summarized in Table 2. A composite foaming agent, PM-D50, was used for foam generation.

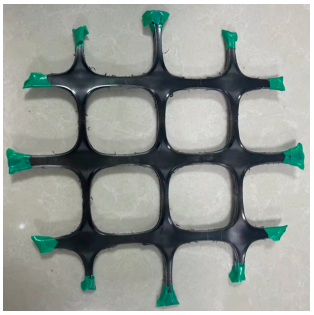


Figure 1. Bi-directional plastic geogrid.

Table 1. Key properties of the geogrid.

Model	Mesh Size (mm)	Tensile Strength (kN/m)		Elongation at Break (%)	
		Vertically	Orthogonal	Vertically	Orthogonal
TGSG50-50	33 × 33	55.8	60.3	6.3	7.6

Table 2. Physical and mechanical properties of the cement.

Specific Surface Area (m^2/kg)	Density (kg/m^3)	Normal Consistency/%	Setting Time/min		Compressive Strength (MPa)	Flexural Strength (MPa)
			Initial Setting	Final Setting		
359	3100	28.5	230	294	5.60	2.72

2.2. Specimen Preparation

To investigate the effects of wet density and the number of geogrid reinforcement layers, specimens were prepared with three different wet densities (600, 700, and 800 kg/m^3) and four different numbers of geogrid layers (0, 1, 2, and 3) [45]. Since this study focuses on the dynamic characteristics of GRFLS, the water–cement ratio was kept constant at 0.55 for all mixes, as outlined in Table 3. During the preparation of the GRFLS specimens, the pre-cut geogrids were first fixed inside cylindrical molds measuring 150 mm in diameter and 300 mm in height using thin iron wires that do not affect the specimen's properties. The arrangement of the geogrid layers is illustrated in Figure 2. Subsequently, the freshly mixed FLS was poured into the molds in accordance with the specified mix proportions. The specimens were then demolded after curing and allowed to harden completely, one or two specimens were prepared for each condition.

Table 3. Proportions of FLS mix.

Wet Density (kg/m^3)	Cement Content (kg/m^3)	Water Content (kg/m^3)	Foam Content (kg/m^3)	Water–Cement Ratio
600	365	201	34	0.55
700	432	237	31	
800	498	274	28	

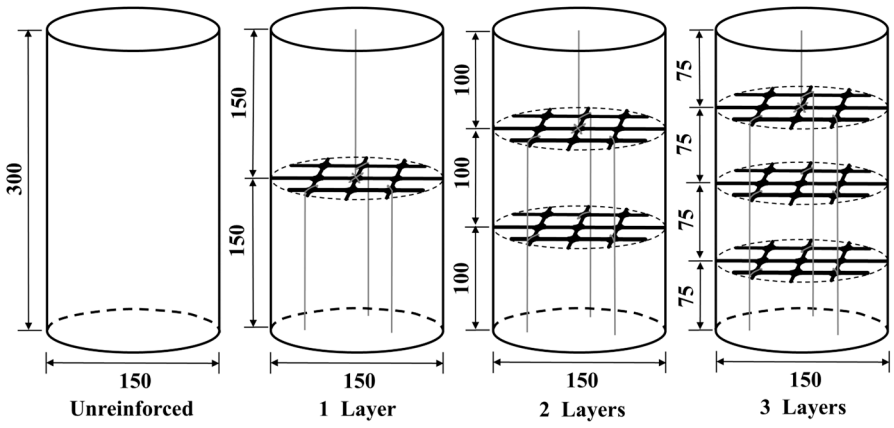


Figure 2. Schematic diagram of the geogrid arrangement in the specimen (unit: mm).

2.3. Test Apparatus

A schematic of the DJSZ-100D dynamic–static triaxial testing system is shown in Figure 3. The test setup primarily consists of a main frame, a hydraulic power station, a confining pressure chamber, a test machine control system, and a cooler. The data acquisition and control software automatically collected test data and controlled the loading device to apply axial load. A stress-controlled, automatically graded application of dynamic

stress was adopted as the loading mode. The main technical parameters of the system are: maximum axial static load of 500 kN and maximum axial dynamic load of 200 kN; confining pressure loading range: 0–2 MPa; displacement measurement range: 0–300 mm; amplitude: 0.1–5 mm; axial excitation frequency range: 0.1–10 Hz.

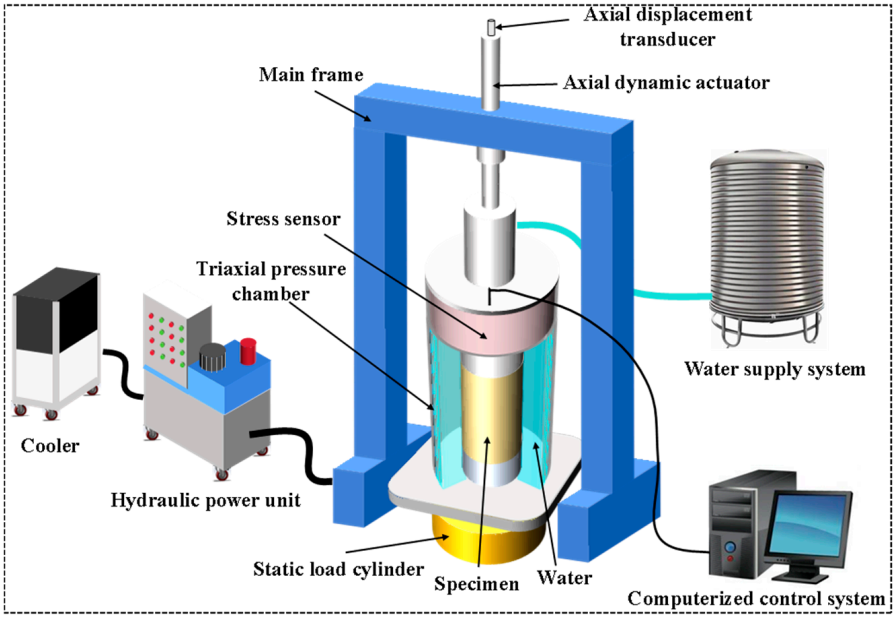


Figure 3. DJSZ-100D dynamic–static triaxial testing system.

The dynamic triaxial tests employed cylindrical specimens with a diameter of 15 cm and a height of 30 cm, resulting in a height-to-diameter ratio of 2. Since the specimen was immersed in a water-filled pressure chamber during the test, a rubber membrane was used to seal the prepared specimen and prevent water influence before it was placed on the base. Since the specimen was immersed in a water-filled pressure chamber during triaxial testing, the prepared specimen was sealed with a rubber membrane and placed on the base to prevent water from affecting the specimen. A schematic of the GRFLS specimen for the triaxial test is shown in Figure 4.



Figure 4. Specimen of GRFLS for triaxial test.

2.4. Test Methods

The multi-stage loading scheme is illustrated in Figure 5. The dynamic triaxial tests were conducted under unconsolidated–undrained (UU) conditions with a confining pressure (σ_c) of 100 kPa. A 3 Hz equivalent sine wave was applied for cyclic loading [46], with 20 cycles per loading stage. The loading levels were defined as the ratio of the dynamic deviator stress (σ_d) to the peak stress (σ_{max}) obtained from static triaxial tests previously completed by the research group. Due to the high initial force capacity of the testing apparatus, the first loading stage commenced at 20% of σ_{max}, with each subsequent stage increasing by 10% of σ_{max} until specimen failure occurred. The detailed multi-stage cyclic loading test program is summarized in Table 4.

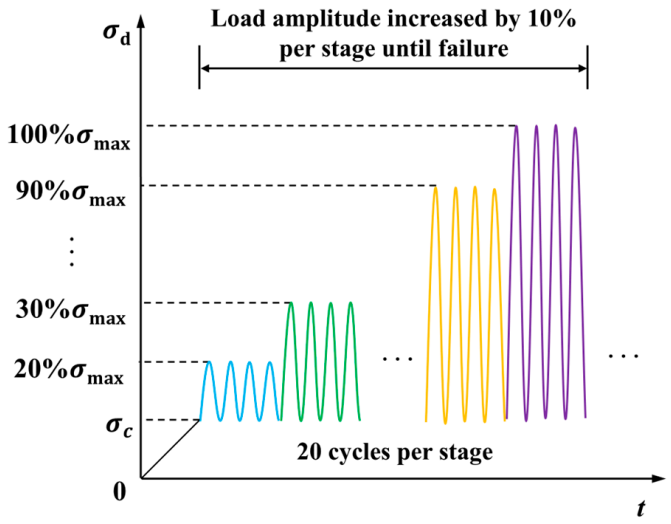


Figure 5. Schematic diagram of the multistage loading.

Table 4. Test program for multistage cyclic loading.

Case Number	Wet Density (kg/m^3)	Number of Reinforcement Layers (Layer)	σ_{max} (MPa)	Amplitude (%)
D1	600	0	1.965	20 → 90
D2	600	1	1.799	20 → 100
D3	600	2	1.786	20 → 100
D4	600	3	1.757	20 → 90
D5	700	0	2.910	20 → 80
D6	700	1	3.279	20 → 80
D7	700	2	2.738	20 → 100
D8	700	3	2.675	20 → 100
D9	800	0	3.275	20 → 80
D10	800	1	3.708	20 → 50
D11	800	2	4.001	20 → 70
D12	800	3	4.510	20 → 50

2.5. Dynamic Deformation Parameters

The typical hysteresis loop shown in Figure 6 can be used to illustrate the evolution of the dynamic elastic modulus and damping ratio of GRFLS. Under cyclic loading, the strain phase consistently lags behind the stress phase during loading and unloading cycles, forming a hysteresis loop. This indicates the hysteresis of dynamic deviator stress relative to dynamic strain, with the primary cause being energy dissipation during the vibration process. In the initial stage of vibration, the impact effect of dynamic stress and viscous damping can cause instability in the hysteresis loop. As the number of vibration cycles increases, the hysteresis loop gradually stabilizes [47]. Experimental data indicated that the hysteresis loop stabilizes after more than 10 cycles. Therefore, the 15th hysteresis loop was selected for the analysis of dynamic deformation parameters in this paper.

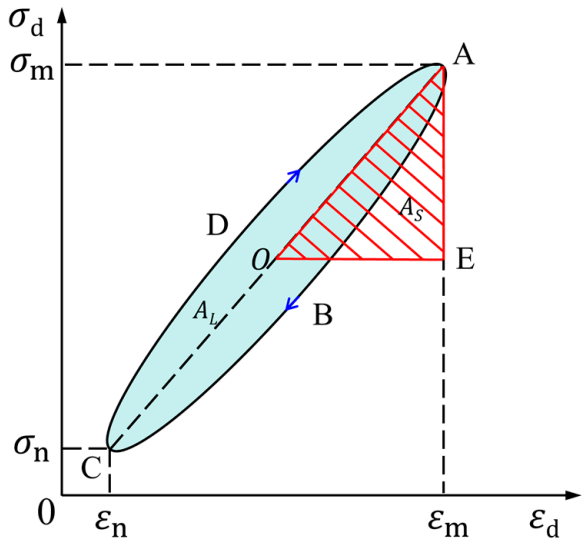


Figure 6. Schematic diagram of a typical hysteresis loop.

The dynamic elastic modulus (E_d) characterizes the ability of GRFLS to resist deformation under dynamic loading. A schematic of a typical hysteresis loop is shown in Figure 6. The E_d is calculated as follows in Equation (1):

$$E_d = \frac{\sigma_m - \sigma_n}{\varepsilon_m - \varepsilon_n} \quad (1)$$

where E_d is the dynamic elastic modulus (MPa); σ_m and σ_n are the maximum and minimum dynamic deviator stresses in the hysteresis loop (MPa), respectively; ε_m and ε_n are the dynamic strains corresponding to the maximum and minimum dynamic stresses, respectively (%); and ε_d is the dynamic strain (%).

The damping ratio (λ) reflects the proportion of energy dissipated due to damping when a cyclic dynamic load is applied to the specimen. It characterizes the ratio of energy lost to the energy input during one complete loading cycle [48]. A typical hysteresis loop is shown in Figure 6. The λ is calculated as follows in Equation (2):

$$\lambda = \frac{A_L}{4\pi A_S} \quad (2)$$

where λ is the damping ratio; A_L is the area enclosed by the hysteresis loop ABCDA; and A_S is the area of the triangle AOE in the upper part of the loop.

3. Test Results and Discussion

3.1. Failure Mode

The failure modes of specimens subjected to multi-stage cyclic loading in dynamic triaxial tests are shown in Figure 7. Unreinforced specimens exhibited characteristics of penetrating cracks and crushing failure. In contrast, in reinforced specimens, the geogrids hindered the vertical propagation of cracks, causing the failure mode to shift to localized damage at the ends, thereby effectively maintaining the overall integrity of the specimen—cracked but not disintegrated. As the number of reinforcement layers increased, the integrity of the specimens improved progressively. However, the difference in elastic modulus between the geogrid and the matrix, combined with boundary effects, made the interfaces more susceptible to shear cracks. Although multi-layer reinforcement suppressed the penetration of longitudinal cracks, it increased the risk of transverse shear failure due to the redistribution of dynamic loads. When the wet density increased from 600 kg/m^3 to

800 kg/m^3, the failure mode of the specimens transitioned from predominantly progressive plastic damage to marked brittle failure characteristics. This is because the increase in wet density of the FLS led to a decrease in porosity and a thickening of the pore walls, reducing its capacity for plastic deformation.

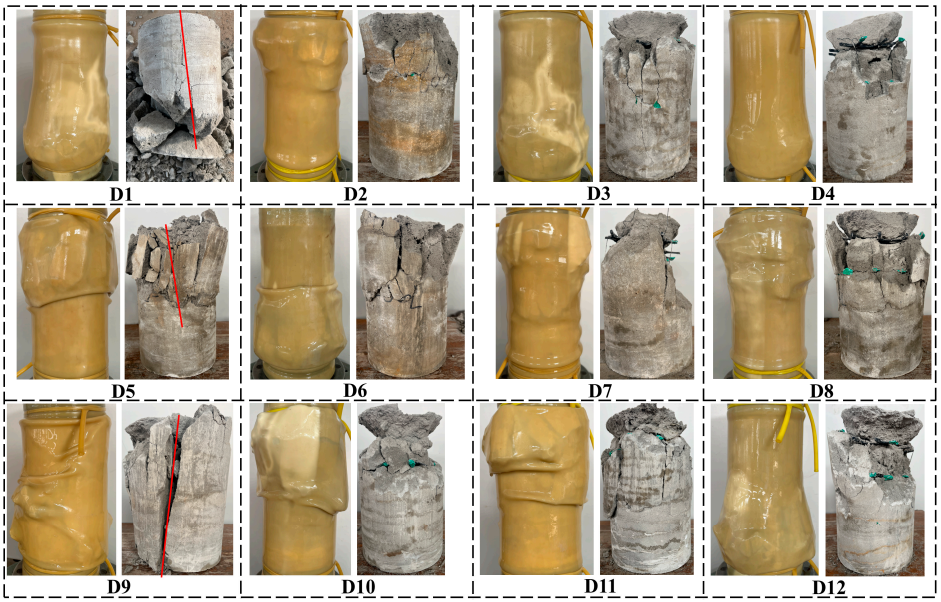


Figure 7. Failure modes of specimens subjected to multistage cyclic dynamic triaxial loading.

3.2. Analysis of Backbone Curve Characteristics

In existing research, the three most commonly used expressions for the backbone curve are the Hardin–Drnevich model (H-D model) [49], the Ramberg–Osgood model [29], and the Davidenkov model [50]. Assuming the GRFLS behaves as a viscoelastic medium, and considering that the H-D model parameters are relatively easier to obtain and its application is widespread, the H-D model was selected to analyze the backbone curve of GRFLS under multi-stage cyclic loading. Based on viscoelastic theory, the H-D model characterizes the nonlinearity and hysteresis of the dynamic deviator stress–strain relationship in soils through equivalent dynamic elastic modulus and equivalent damping ratio. It establishes empirical functions for the E_d and the λ, expressed as $E_d = E(\varepsilon_d)$ and $\lambda = \lambda\ (\varepsilon_d)$ [51].

Under multi-stage cyclic loading, a schematic of the typical backbone curve for dynamic deviator stress versus dynamic strain is shown in Figure 8. The backbone curve is formed by connecting the vertices of the 15th hysteresis loop from each loading stage, describing the dynamic deviator stress–strain relationship of the GRFLS under dynamic loading.

The results of the multi-stage cyclic tests were analyzed using the H-D model, expressed as Equation (3):

$$\sigma_d = \frac{\varepsilon_d}{\frac{1}{E_0} + \frac{\varepsilon_d}{\sigma_y}} = \frac{\varepsilon_d}{u + v\varepsilon_d} \tag{3}$$

where σ_y is the maximum axial dynamic deviator stress (MPa), and u and v are fitting parameters.

In Figure 8, the horizontal coordinate corresponding to the intersection point of the slope line of E_0 and the horizontal line of σ_y is defined as the reference strain ε_r, leading to Equation (4):

$$\varepsilon_r = \frac{\sigma_y}{E_0} \tag{4}$$

The physical meanings of the fitting parameters u and v are given by Equation (5):

$$u = \frac{1}{E_0},\ v = \frac{1}{\sigma_y},\ \varepsilon_r = \frac{u}{v} \tag{5}$$

The H-D model was fitted to the experimental data. The resulting fitting parameters, initial dynamic elastic modulus, and reference strain are summarized in Table 5. The minimum value of the coefficient of determination (R^2) was 0.984, indicating that the H-D model effectively captures the variation in the backbone curve of the GRFLS.

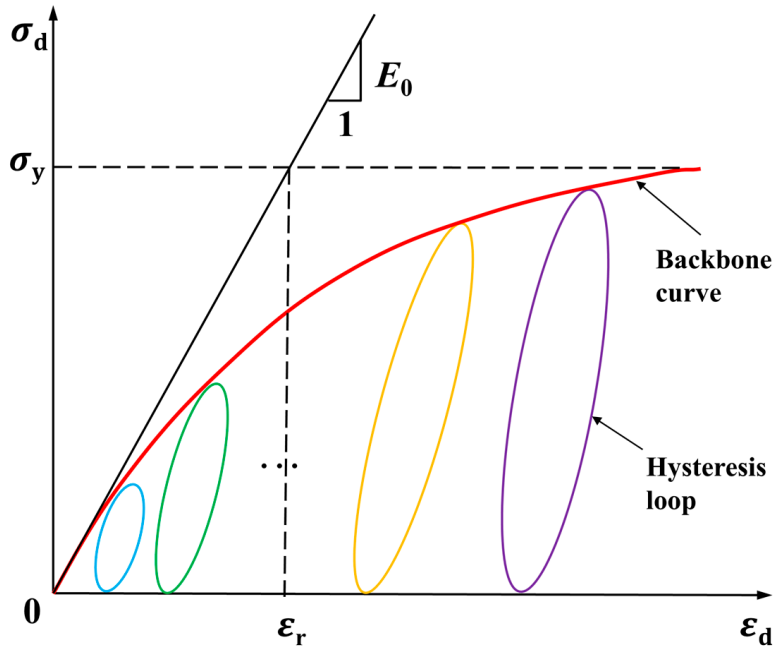


Figure 8. Schematic diagram of the typical backbone curve for dynamic deviator stress versus strain.

Table 5. Fitting results of GRFLS using the H-D model.

Number	u	v	R^2	E_0 (MPa)	ε_r (%)
D1	0.494	0.588	0.998	202.400	0.840
D2	0.523	0.613	0.997	191.234	0.853
D3	0.530	0.566	0.996	188.601	0.937
D4	0.503	0.657	0.995	198.989	0.765
D5	0.358	0.245	0.984	279.166	1.460
D6	0.353	0.345	0.996	283.511	1.023
D7	0.352	0.298	0.999	283.704	1.184
D8	0.348	0.294	0.992	287.356	1.182
D9	0.270	0.241	0.999	370.288	1.121
D10	0.274	0.199	0.999	365.110	1.379
D11	0.280	0.218	0.999	357.411	1.286
D12	0.277	0.167	0.999	361.376	1.659

The influences of the number of reinforcement layers and wet density on the backbone curve are shown in Figures 9 and 10. In the initial stage, the GRFLS exhibited favorable elastic deformation characteristics, with the dynamic strain increasing gradually and the backbone curve rising linearly, indicating predominantly elastic behavior. As the wet density increased, the dynamic strain in the initial stage increased from 0.1% to 0.25% [52]. With further increase in dynamic deviator stress, the specimen began to undergo elastoplastic deformation, accompanied by a deceleration in the growth rate of the dynamic deviator stress until eventual failure occurred.

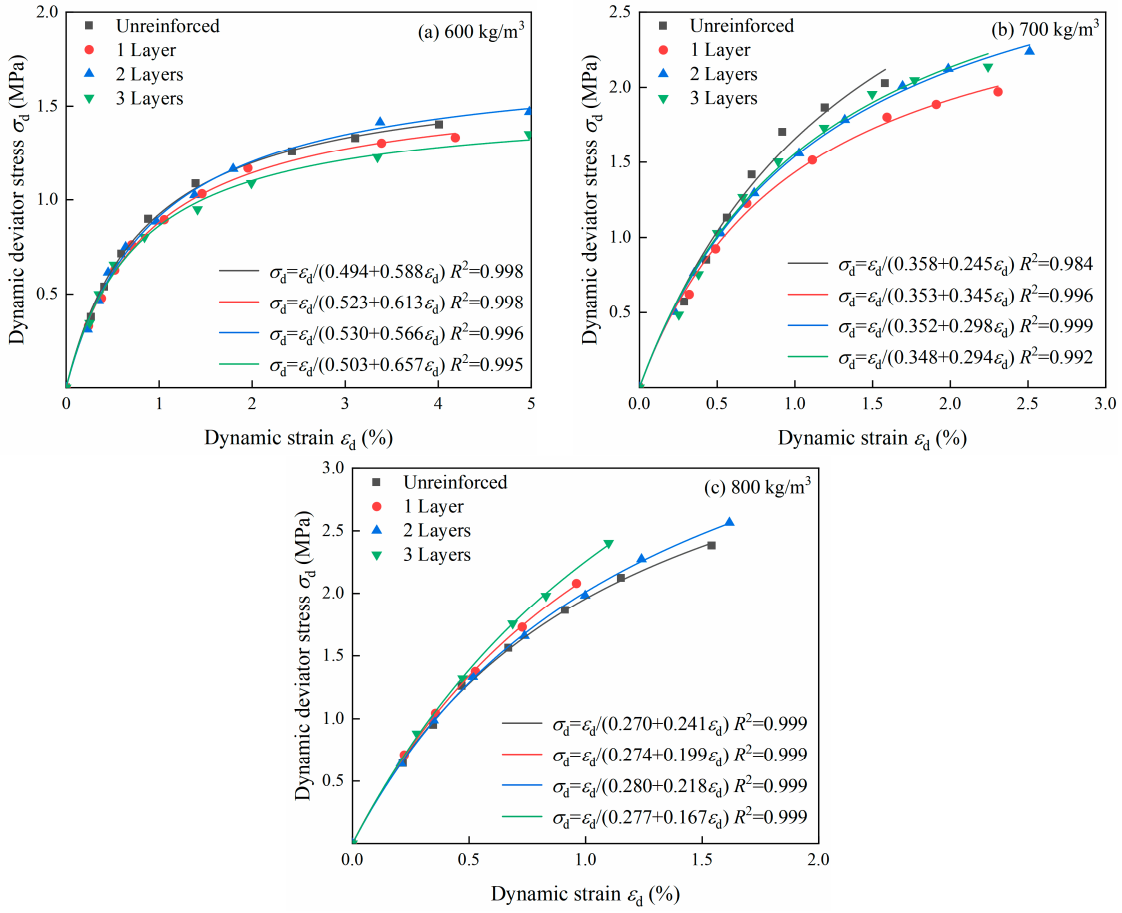


Figure 9. Influence of the number of reinforcement layers on the backbone curves of GRFLS: (**a**) 600 kg/m^3; (**b**) 700 kg/m^3; (**c**) 800 kg/m^3.

Figure 9 illustrates the influence of the number of geogrid layers on the backbone curve. When two reinforcement layers were used, the dynamic deviator stress of the FLS increased significantly with greater dynamic strain. In contrast, the effect of one layer was similar to that of three layers, with the latter even showing a reduction in dynamic deviator stress in some cases. Within the dynamic strain range of 0–0.5%, the reinforcing effect of the geogrid was not pronounced. However, when the dynamic strain reached 1%, the strengthening effect became evident, indicating that the inclusion of geogrids provides limited improvement in dynamic deviator stress under small-strain conditions [53]. The reinforcing system effectively enhances the overall dynamic deviator stress only after the specimen reaches a critical deformation threshold. Since the FLS forms an integrated solid after curing, the incorporation of geogrids may, due to boundary effects, partially compromise this integrity. Under different numbers of reinforcement layers, some specimens consequently exhibited a decrease in dynamic deviator stress.

The influence of wet density on the backbone curve is shown in Figure 10. Under the same number of reinforcement layers, an increase in wet density led to a gradual decrease in dynamic strain, while the sustained dynamic deviator stress increased progressively. This indicates that higher wet density promotes the formation of more hydration products through cement hydration, resulting in reduced foam content and fewer air voids within the specimen. Consequently, stronger bonding forces develop between solid particles, enhancing the deformation stiffness and brittleness of the material. The increased stiffness hinders the relative movement of solid particles, thereby improving the resistance to deformation.

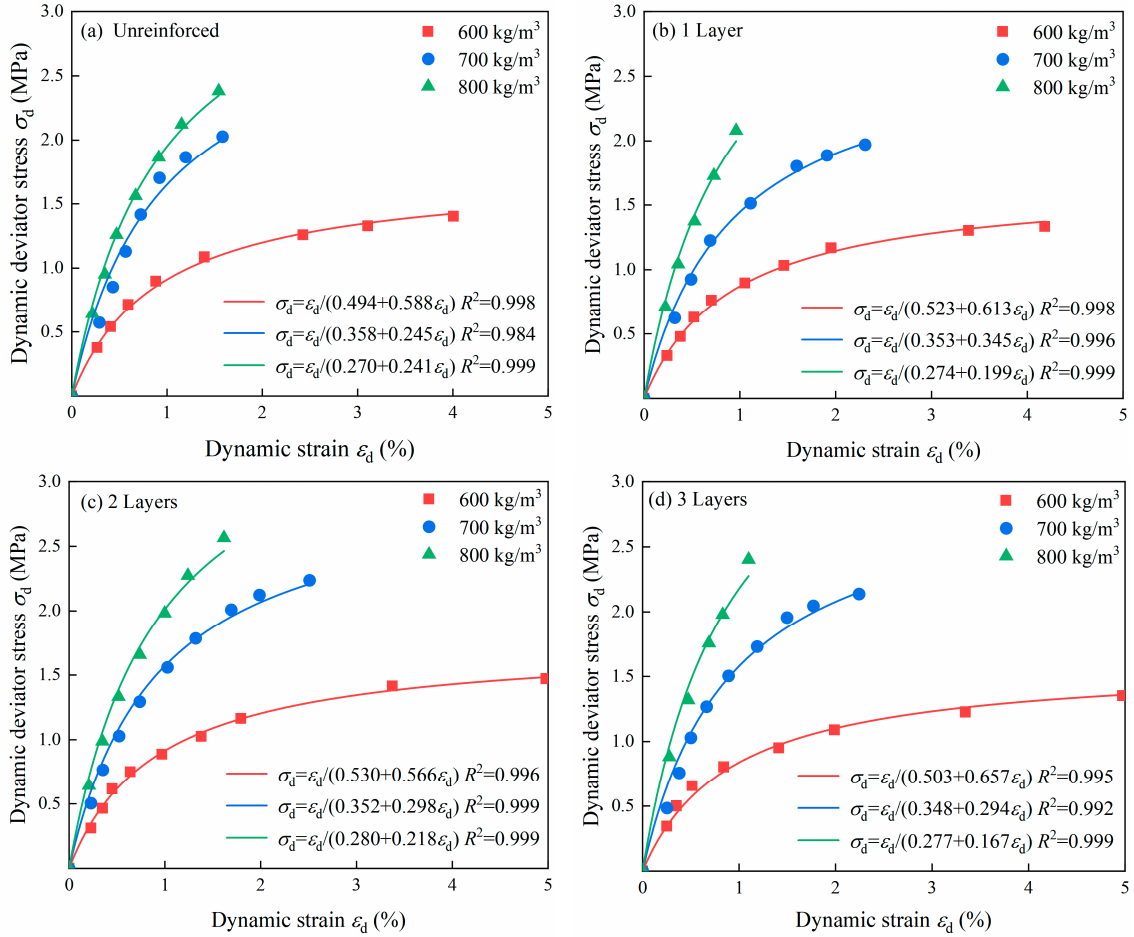


Figure 10. Influence of wet density on the backbone curves of GRFLS: (**a**) unreinforced; (**b**) 1 layer; (**c**) 2 layers; (**d**) 3 layers.

3.3. Analysis of Mechanical Parameters

3.3.1. Dynamic Strength

Dynamic strength is defined as the dynamic deviator stress at failure under cyclic loading, reflecting the material's ability to resist staged cyclic loads [29]. A comparative analysis was conducted with the static peak strength (hereinafter referred to as static strength) obtained from related static triaxial tests completed by our research group. The static and dynamic strengths of the GRFLS are shown in Figure 11.

The inclusion of geogrids enhances the dynamic strength of the FLS, primarily by restraining crack propagation and redistributing the dynamic deviator stress. Unreinforced specimens exhibited a significant decrease in dynamic strength compared to their static strength due to accumulated damage under repeated dynamic loading [28]. This reduction was particularly notable at a wet density of 800 kg/m^3, where the dynamic strength decreased by a maximum of 1.52 MPa. In contrast, the damage accumulation rate was slowed down in the reinforced specimens.

When the wet density increased from 600 kg/m^3 to 700 kg/m^3, the dynamic strength increased by 51%. However, when the density further increased to 800 kg/m^3, the strength increase dropped to 13%. This indicates that specimens with higher wet density, characterized by reduced porosity and a higher proportion of hydrated solids, experience a weakened energy absorption capacity and an enhanced tendency for brittle failure. Consequently, the rate of strength gain diminishes.

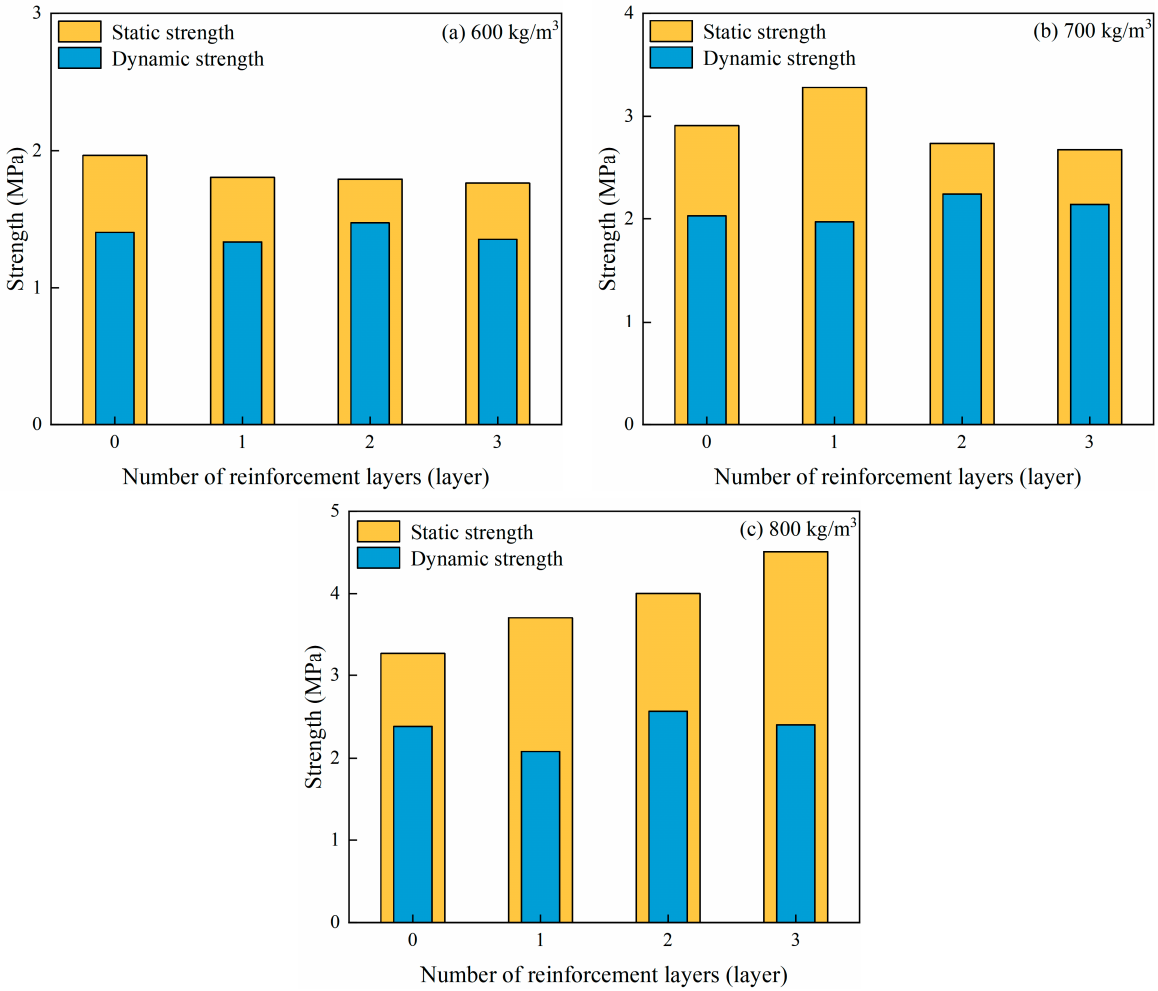


Figure 11. Static and dynamic strengths of GRFLS: (**a**) 600 kg/m^3; (**b**) 700 kg/m^3; (**c**) 800 kg/m^3.

To investigate the influence of the number of reinforcement layers on the strength of the FLS, the reinforced strength stress ratio (SR), as defined by Tang F et al. [53], was adopted:

$$\mathrm{SR} = \frac{\sigma_{\mathrm{dre}}}{\sigma_{\mathrm{dun}}} \tag{6}$$

where SR is the reinforced strength stress ratio; σ_{dre} is the dynamic strength of the reinforced specimen (MPa); and σ_{dun} is the dynamic strength of the unreinforced specimen (MPa).

The relationship between the reinforced strength stress ratio and the number of reinforcement layers is shown in Figure 12. The SR value of the FLS initially increases and then decreases as the number of reinforcement layers rises. The maximum SR is achieved with two reinforcement layers. In contrast, the improvement in dynamic strength is relatively minor with one or three layers, with some cases even exhibiting a reduction in dynamic strength. This indicates that two reinforcement layers provide the optimal enhancement effect on the dynamic strength of the specimens, offering a reference for practical engineering design optimization. Adopting this optimal number helps extend the service life of the reinforced structure while ensuring cost-effectiveness. Furthermore, specimens with a wet density of 700 kg/m^3 consistently demonstrate higher SR values compared to those with other wet densities. This suggests that the reinforcing effect is most pronounced in enhancing the dynamic strength for specimens with a wet density of 700 kg/m^3.

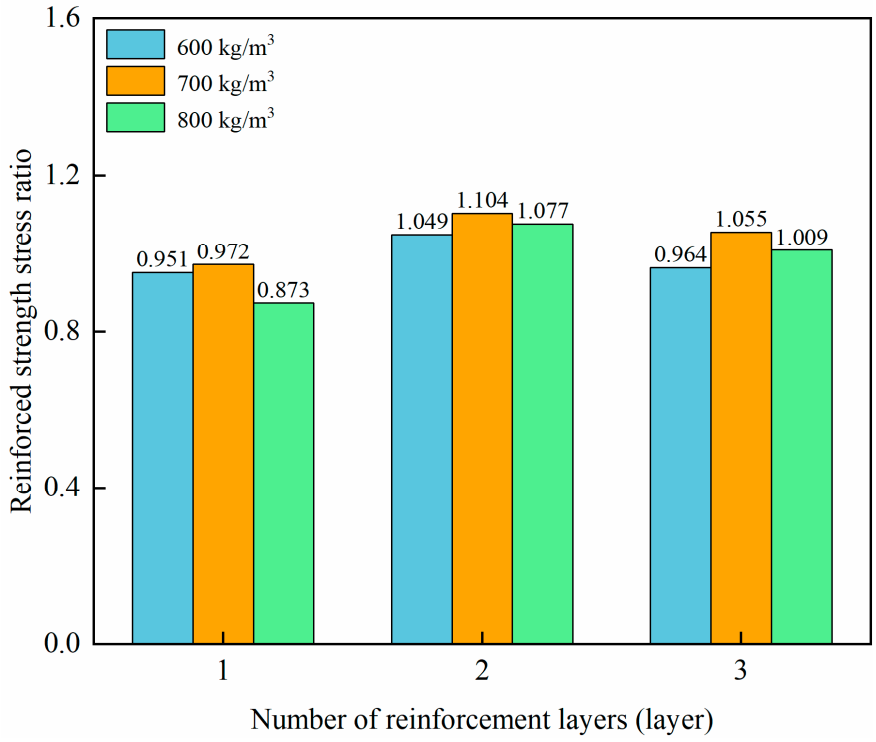


Figure 12. Relationship between SR and number of reinforcement layers.

3.3.2. Dynamic Elastic Modulus

The influence of the number of reinforcement layers on the E_d-ε_d of GRFLS is shown in Figure 13. When the wet density remained constant, the E_d of specimens reinforced with one and two layers was greater than that of unreinforced specimens and those with three layers. The values for the unreinforced and three-layer reinforced specimens were relatively close. When the number of reinforcement layers was kept constant, the dynamic elastic modulus increased with the wet density of the FLS. This is because a higher wet density corresponds to a greater proportion of cementitious solids and stronger internal cohesion, which enhances the specimen's resistance to deformation and leads to a gradual increase in the E_d. Therefore, an appropriate number of geogrid layers can effectively disperse dynamic loads into the FLS, improving the specimen's resistance to deformation and resulting in a significant increase in its E_d.

3.3.3. Damping Ratio

The influence of the number of reinforcement layers on the λ-ε_d of GRFLS is shown in Figure 14. When the wet density remained constant, the growth rate of the damping ratio exhibited significant convergence across different numbers of reinforcement layers. The incorporation of geogrids does not alter the microstructure of the FLS; consequently, its effect on improving energy dissipation characteristics is limited. At small dynamic strains, the damping ratio increased gradually, as the geogrid reinforcement system had not yet significantly influenced the micromechanical response of the material. At larger dynamic strains, damage mechanisms such as the propagation of microcracks and interfacial slip were progressively activated within the specimen, leading to a continued increasing trend in the damping ratio. When the number of reinforcement layers was kept constant, a decrease in wet density increased porosity. Under dynamic loading, greater volumetric compression and higher dynamic strain induce plastic deformation, thereby absorbing more energy and causing the damping ratio to increase gradually.

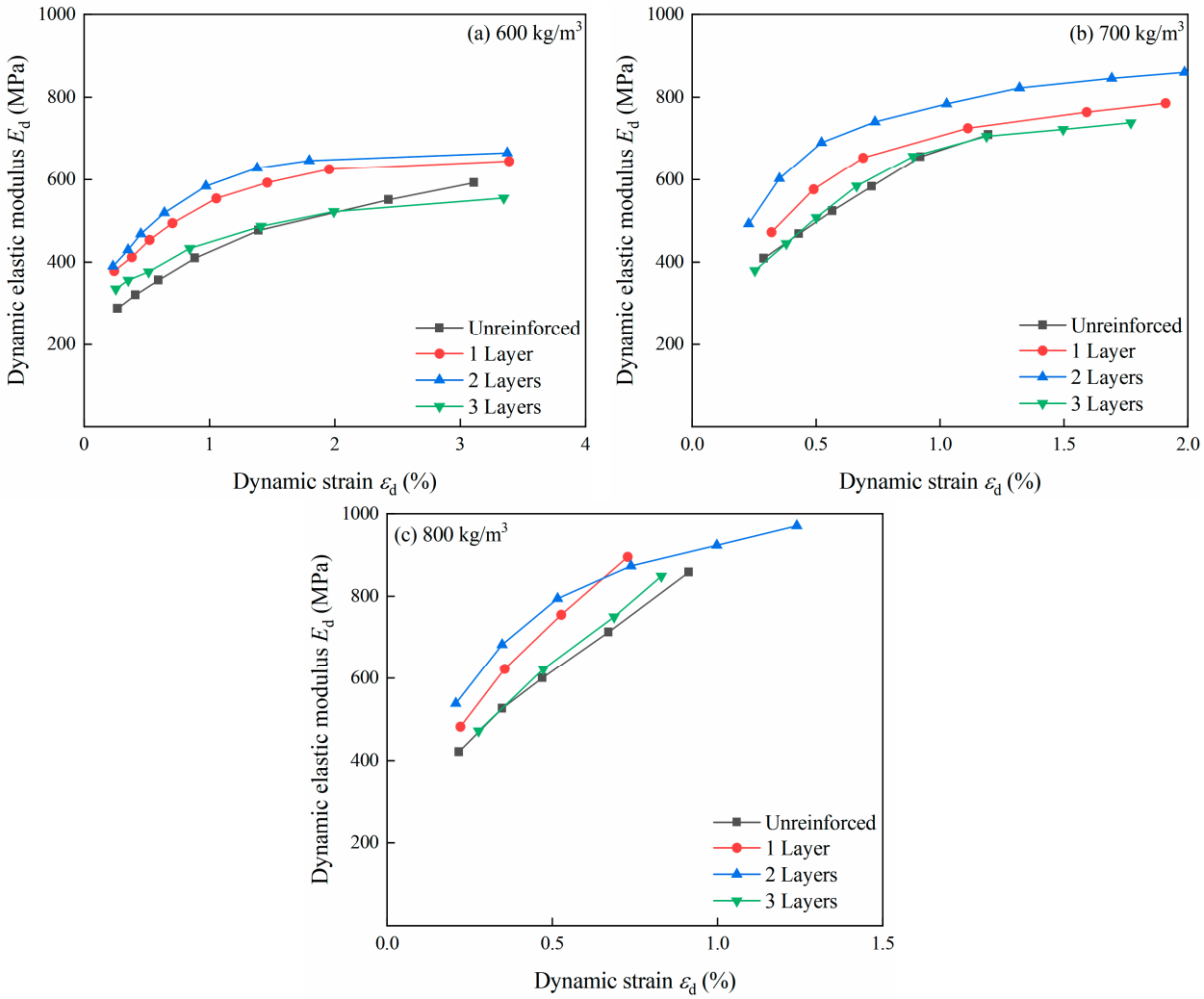


Figure 13. Influence of the number of reinforcement layers on the E_d-ε_d of GRFLS: (**a**) 600 kg/m^3; (**b**) 700 kg/m^3; (**c**) 800 kg/m^3.

3.4. Establishment and Validation of Mechanical Parameter Models

3.4.1. Enhanced Model for Dynamic Elastic Modulus

As shown in Figure 13, the E_d of the GRFLS increases with increasing dynamic strain under the influence of wet density and the number of reinforcement layers. This trend contrasts with the findings of Xu T et al. [54], who observed that the E_d of soils generally decreases with increasing dynamic strain. The behavior of GRFLS can be attributed to its internal microstructure. During the initial loading stage, the applied dynamic deviator stress is relatively small. The presence of numerous pores and microcracks within the FLS facilitates an increase in dynamic strain, resulting in a lower E_d initially. As the number of loading cycles and the amplitude increase, the specimen becomes progressively compacted, leading to a reduction in porosity. Consequently, a greater proportion of solid particles participate in bearing the dynamic load, generating smaller dynamic strains and causing the E_d to increase gradually. This is consistent with the research findings of Li M et al. [33].

The initial dynamic elastic modulus (E_0), which reflects the material's ability to resist dynamic loads in its initial state, is an essential parameter for establishing the enhanced dynamic elastic modulus model. It is defined as the dynamic elastic modulus when the dynamic strain approaches zero. The hyperbolic form of the backbone curve representing

the dynamic deviator stress versus dynamic strain under cyclic loading, as described previously by the H-D model, serves as the foundation and is given by Equation (7):

$$\frac{E_d}{E_0} = \frac{1}{1 + \frac{\varepsilon_d}{\varepsilon_r}} \tag{7}$$

where E_0 is the initial dynamic elastic modulus (MPa).

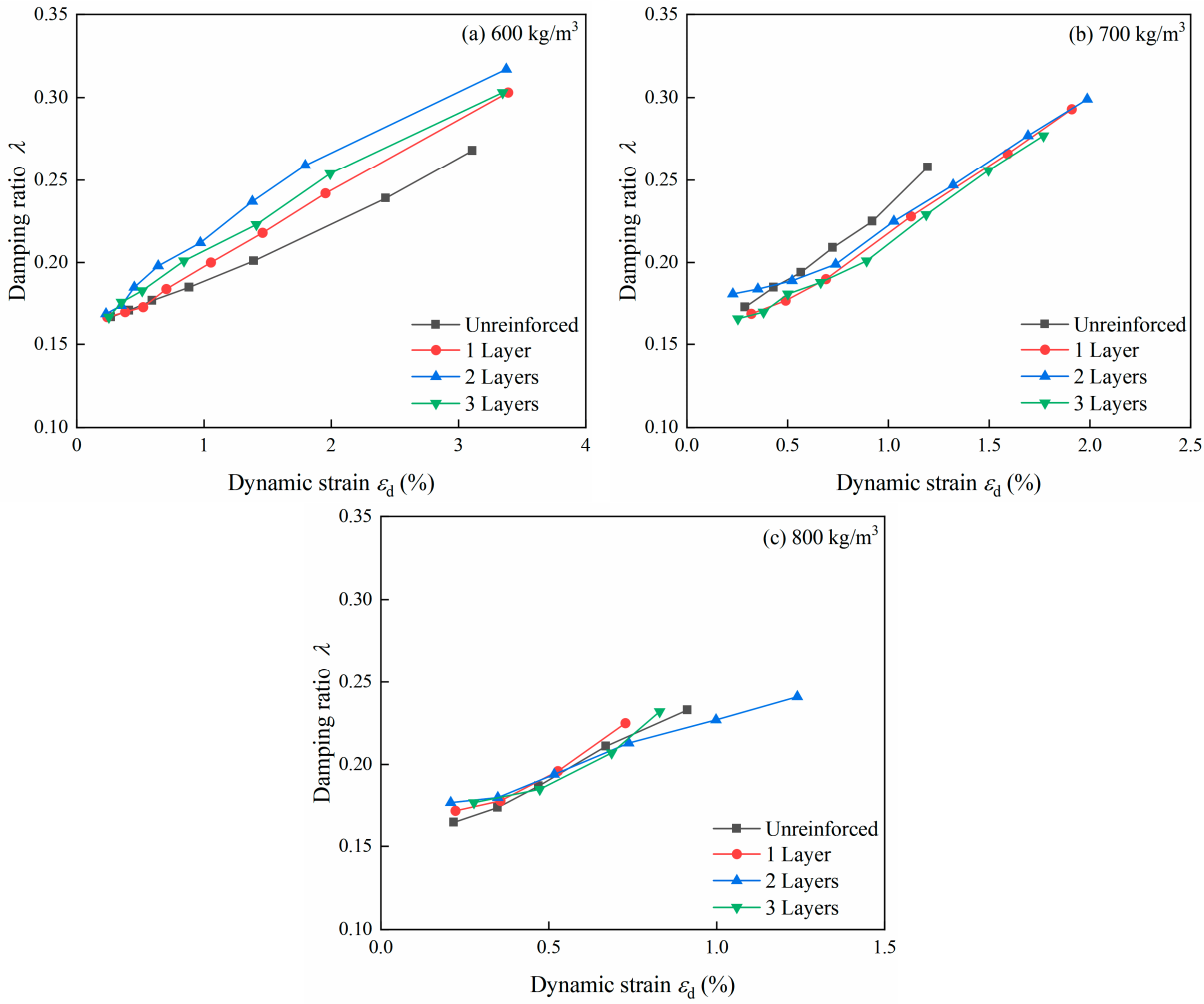


Figure 14. Influence of the number of reinforcement layers on the λ_d-ε_d of GRFLS: (**a**) 600 kg/m^3; (**b**) 700 kg/m^3; (**c**) 800 kg/m^3.

Based on the results shown in Figure 13, a significant increasing relationship was observed between the E_d and the ε_d. This trend contrasts with the decreasing function described by the H-D model for the Ed relative to ε_d. Consequently, a modification to the H-D model is necessary. When the wet density increased from 600 kg/m^3 to 800 kg/m^3, the E_0 of the GRFLS increased by an average of 45.4%. Similarly, when the number of reinforcement layers increased from zero to two, the E_0 increased by an average of 15.6%. Considering the influence of wet density and the number of reinforcement layers on the E_0, a multiple linear regression equation for the E_0 was established, as shown in Equation (8). The relationship between the E_0, ρ, and X is illustrated in Figure 15.

$$E_0 = 0.841\rho - 0.751X - 306.952 \tag{8}$$

where ρ is the wet density (kg/m^3) and X is the number of reinforcement layers (layer).

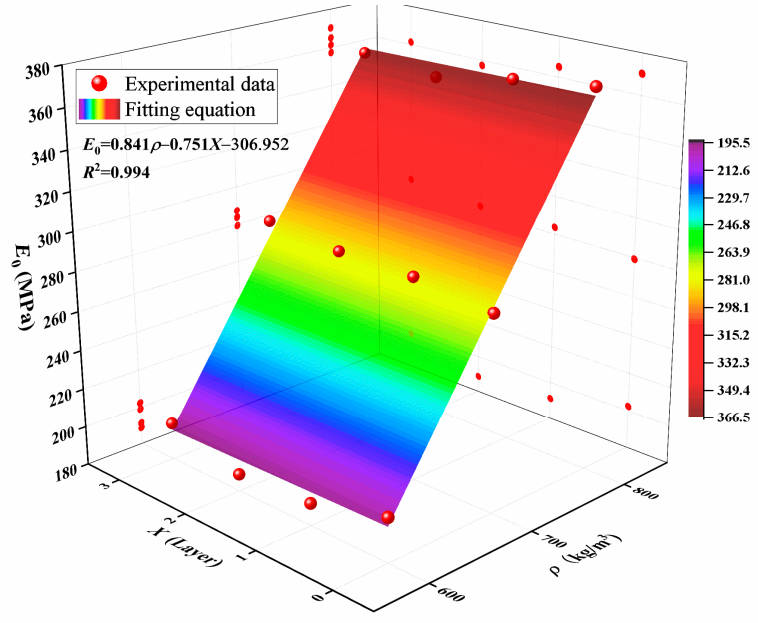


Figure 15. Relationship between the E_0, ρ, and X.

An enhanced model describing the relationship between the dynamic elastic modulus and dynamic strain was established. The curve representing the ratio of the dynamic elastic modulus to the initial dynamic elastic modulus versus dynamic strain is shown in Figure 16. This relationship is quantitatively described by Equation (9):

$$\frac{E_d}{E_0} = 2.438\varepsilon_d{}^{0.271} \quad (9)$$

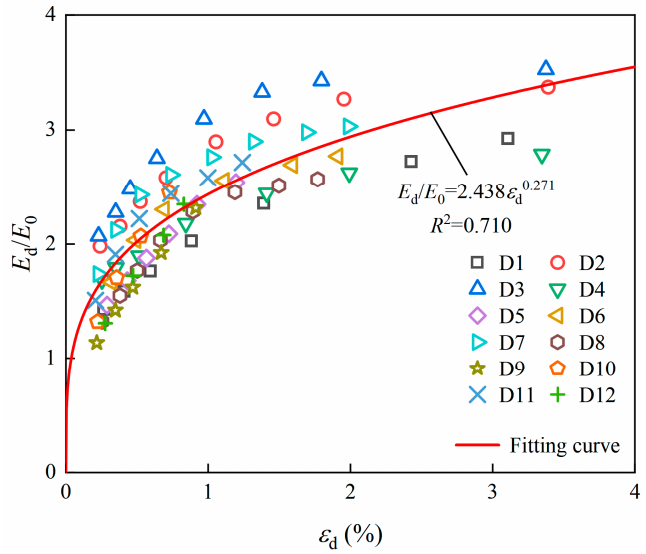


Figure 16. Relationship between the E_d/E_0 and dynamic strain.

To validate the accuracy of the model, the predicted dynamic elastic modulus of the GRFLS was calculated using Equations (8) and (9). A comparison between the calculated and measured results for specimens with one reinforcement layer is shown in Figure 17. The calculated values show a high degree of consistency with the measured results. Therefore, the established enhanced model for the E_d can accurately reflect the deformation characteristics of GRFLS under medium- to large-strain conditions.

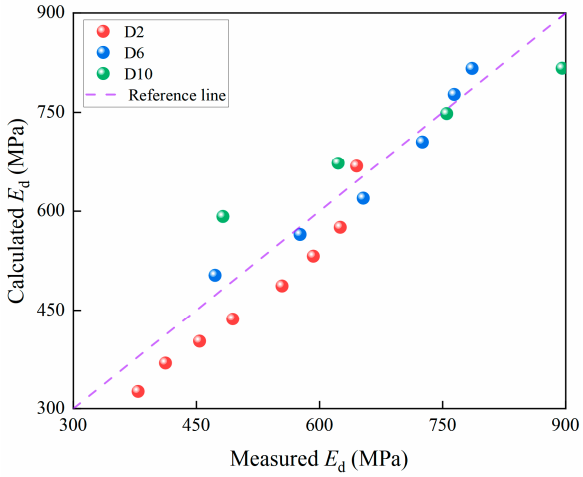


Figure 17. Comparison between calculated and measured E_d for specimens with one reinforcement layer.

3.4.2. Predictive Model for Damping Ratio

As shown in Figure 14, the damping ratio of the GRFLS gradually increases with dynamic strain until reaching its maximum value. Overall, the incorporation of geogrids increased the maximum damping ratio (λ_{max}) by an average of 9.4%. Specifically, specimens with two reinforcement layers exhibited an average increase of 12.9% in the λ_{max} compared to unreinforced specimens. Conversely, for every 100 kg/m^3 increase in wet density, the λ_{max} decreased by 5.4% and 17.4%, respectively. Considering the influence of both wet density and the number of reinforcement layers on the λ_{max}, a multiple linear regression equation was established, as shown in Equation (10). The relationship between the λ_{max}, ρ, and X is presented in Figure 18.

$$\lambda_{max} = 0.002\rho - 1.563 \times 10^{-6}\rho^2 + 0.046X - 0.012X^2 - 0.266 \quad (10)$$

where λ_{max} is the maximum damping ratio. ρ ranges from 600 to 800 kg/m^3.

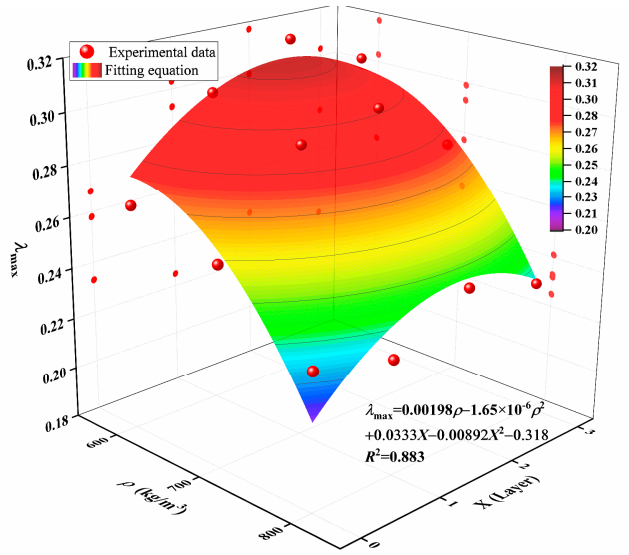


Figure 18. Relationship between λ_{max}, ρ, and X.

The relationship between the ratio of the damping ratio to the maximum damping ratio and the dynamic strain is shown in Figure 19. Under different wet densities, this ratio

increases linearly with dynamic strain, which is represented by Equation (11) based on linear fitting results:

$$\frac{\lambda}{\lambda_{\max}} = r\varepsilon_d + s \tag{11}$$

where r and s are fitting parameters, the values of which are listed in Table 6.

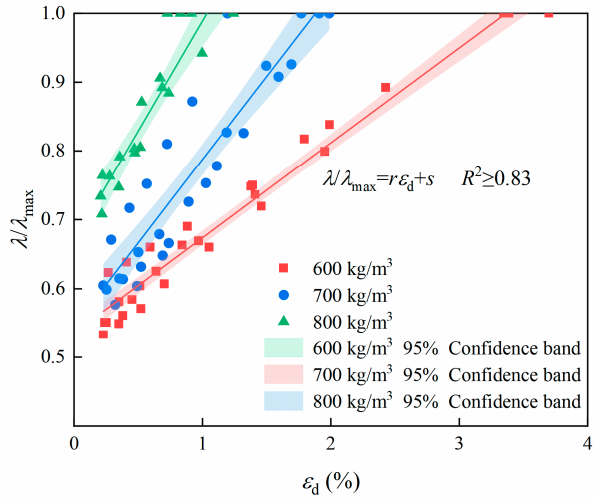


Figure 19. Relationship between $\lambda/\lambda_{\max}$ and dynamic strain.

Table 6. Values of fitting parameters r and s.

Wet Density (kg/m^3)	r	s	R^2
600	0.138	0.536	0.968
700	0.242	0.546	0.841
800	0.320	0.669	0.832

To validate the accuracy of the model, the damping ratio of GRFLS was predicted using Equations (10) and (11). A comparison between the calculated and measured damping ratios for specimens with one reinforcement layer is shown in Figure 20. The calculated results show a high degree of consistency with the measured values. Therefore, the established predictive model for the damping ratio can accurately reflect the deformation characteristics of GRFLS under medium to large strain conditions.

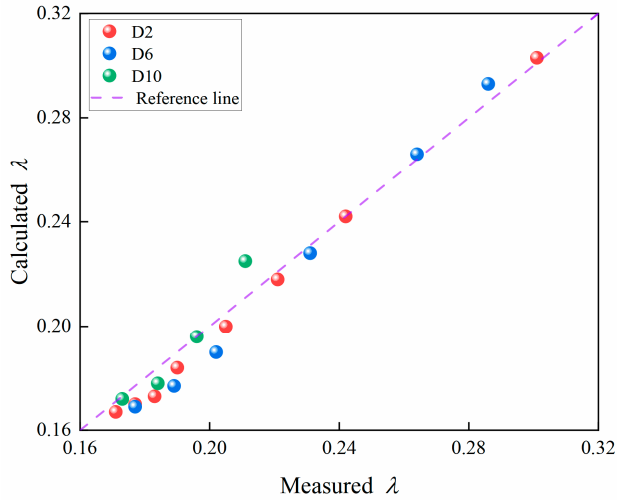


Figure 20. Comparison between calculated and measured λ for specimens with one reinforcement layer.

3.5. Discussion

FLS is commonly used as fill material for shallow structures such as subgrades and abutment backfills, where it primarily bears the overlying self-weight and the relatively low lateral stresses induced by vehicle loads. Selecting a single confining pressure representative of this shallow stress level allows the study to focus on the reinforcement effect itself while avoiding interference from the superimposed confining pressure; further analysis under high-confining-pressure conditions can be carried out in subsequent work. The loading frequency was set at 3 Hz, which directly corresponds to the typical frequency range of road and railway traffic loads, making the study more engineering-oriented. The water–cement ratio was determined as a representative mix proportion based on the target wet density and strength requirements. Fixing this parameter ensures the stability of the base properties of the foamed lightweight soil, thereby highlighting the independent effects of the number of reinforcement layers and wet density.

The backbone curves of the GRFLS obtained from the tests exhibit good hyperbolic characteristics and can be accurately described by the Hardin–Drnevich model, which is consistent with the dynamic constitutive behavior of unreinforced FLS and other lightweight cement-based materials under cyclic loading. Unlike the dynamic elastic modulus of expanded polystyrene (EPS) lightweight soil [55], which gradually decreases with increasing dynamic strain, the dynamic elastic modulus of GRFLS gradually increases with increasing dynamic strain.

Both the established dynamic elastic modulus model and the damping ratio prediction model were quantitatively validated against the test data. The coefficient of determination R^2 for the dynamic elastic modulus model exceeded 0.7, and the average relative error under various test conditions was within 10%; for the damping ratio model, R^2 exceeded 0.8 with an average relative error within 12%. This level of accuracy falls within the acceptable range for empirical dynamic models in geotechnical engineering and can reasonably reflect the influence of wet density and the number of reinforcement layers on the dynamic parameters.

FLS, owing to its lightweight nature, can significantly reduce the self-weight of structures and the additional stress on the foundation; however, low density is often accompanied by low dynamic stiffness and energy dissipation capacity, which restricts the application of such materials in dynamic environments such as traffic and seismic loading. Geogrid reinforcement can not only effectively increase the dynamic elastic modulus but also enable the damping ratio to increase steadily with increasing dynamic strain, endowing the reinforced foamed lightweight soil with favorable potential for vibration energy dissipation. Therefore, this type of reinforced lightweight material can be used in heavy-haul railway subgrades, wall backfills, and for vibration isolation in soil–structure systems [56].

4. Conclusions

This study conducted graded cyclic loading dynamic triaxial tests on GRFLS. Based on the observed failure modes and utilizing the Hardin–Drnevich equivalent linear model, the backbone curve was modified, and the corresponding model parameters were calculated. The influence of various factors on the mechanical parameters was analyzed. Predictive models for the dynamic elastic modulus and damping ratio, capable of characterizing the dynamic deviator stress–strain relationship, were established and validated. The main conclusions are as follows:

1. The inclusion of geogrids effectively restrained the propagation of longitudinal cracks, leading to localized failure. However, multi-layer reinforcement induced interfacial shear cracks due to size effects, while an increase in wet density significantly enhanced the tendency for brittle failure.

2. The backbone curve of GRFLS exhibits a hyperbolic shape, which can be accurately described by the Hardin–Drnevich model, demonstrating typical nonlinearity and hysteresis. The reinforcing effect becomes noticeable after the dynamic strain exceeds 0.5%. As the wet density increases, the dynamic strain gradually decreases, while the dynamic deviator stress increases. An optimal number of two reinforcement layers was identified based on the reinforced strength stress ratio.
3. The dynamic elastic modulus of GRFLS increases with increasing dynamic strain. Compared with the unreinforced condition, the initial dynamic elastic modulus of the specimens with two geogrid layers increased by an average of 15.6%. Reinforcement with one or two layers effectively disperses dynamic loads, and an increase in wet density raises the proportion of cementitious solids. Both factors enhance the dynamic elastic modulus, collectively improving the material's resistance to deformation.
4. The damping ratio of GRFLS increases with increasing dynamic strain. Compared with the unreinforced condition, the maximum damping ratio of the specimens with two geogrid layers increased by an average of 12.9%. The number of reinforcement layers does not significantly affect the growth trend of the damping ratio. Specimens with lower wet density exhibit a higher maximum damping ratio due to greater energy absorption through pore compression. In contrast, higher wet density results in increased material stiffness, reduced energy dissipation, and a lower maximum damping ratio.
5. Based on the Hardin–Drnevich model, under a confining pressure of 100 kPa, a frequency of 3 Hz, and a wet density ranging from 600 to 800 kg/m^3, predictive functions for the dynamic elastic modulus and damping ratio were established using the initial dynamic elastic modulus and the maximum damping ratio. The functions $Ed = E(\varepsilon_d)$ and $\lambda = \lambda(\varepsilon_d)$ effectively represent the dynamic deviator stress–strain relationship of GRFLS, and the models were validated to possess good accuracy.
6. Under cyclic-loading-dominated engineering conditions, appropriately increasing the number of reinforcement layers or raising the wet density can effectively enhance the dynamic elastic modulus of GFLS, thereby improving the deformation resistance of the structure. Moreover, the established predictive model can directly provide a quantitative basis for the engineering design and numerical analysis of reinforced FLS subjected to cyclic loading.

5. Future Work

This study has certain limitations: it has not fully considered the coupled effects of multiple factors such as loading frequency, stress path, and geogrid type, nor has it conducted in-depth durability tests such as wetting–drying and freezing–thawing cycles. Therefore, in follow-up research, systematic multi-factor coupled dynamic triaxial tests will be carried out, focusing on the combined effects of loading frequency, different stress paths, and various geogrid types on the dynamic characteristics of the material. Meanwhile, wetting–drying and freezing–thawing durability tests will be designed, and a durability degradation model will be established by comparing the attenuation laws of the dynamic elastic modulus, damping ratio, and strength before and after the tests. Furthermore, discrete element method (DEM) or finite element method (FEM) numerical simulations will be employed to establish a quantitative relationship between the meso-structure and the macroscopic mechanical properties. In addition, full-scale model tests and long-term field monitoring are planned to verify the engineering applicability of the laboratory test results, thereby providing data support and theoretical guidance for large-scale application.

Author Contributions: Writing—original draft, Y.L. (Yinhe Li); writing—review and editing, Y.L. (Yong Liu); visualization, Y.L. (Yinhe Li); supervision, Y.L. (Yong Liu); methodology, Y.L. (Yong Liu);

software, Y.S.; validation, Y.S.; data curation, Y.S.; project administration, Y.L. (Yong Liu). All authors have read and agreed to the published version of the manuscript.

Funding: This research received no external funding.

Data Availability Statement: The data that used in this study can be required from the corresponding author. The data are not publicly available due to information that could compromise research participant privacy.

Conflicts of Interest: The authors declare no conflicts of interest.

References

1. Amran, Y.H.M.; Farzadnia, N.; Abang Ali, A.A. Properties and applications of foamed concrete; a review. *Constr. Build. Mater.* **2015**, *101*, 990–1005. [CrossRef]
2. Pan, G.; Gong, H.; Sun, Z.; Chen, L.; Liu, Z.; Gao, L. Towards High-Performance Low-Carbon Foam Concrete: A Review on Multi-Component Synergy and Pore Structure Optimization. *J. Build. Eng.* **2026**, *120*, 115570. [CrossRef]
3. Raj, A.; Sathyan, D.; Mini, K.M. Physical and Functional Characteristics of Foam Concrete: A Review. *Constr. Build. Mater.* **2019**, *221*, 787–799. [CrossRef]
4. Junjie, H.; Cai, D.; Su, Q.; Yao, H.; Fan, R.; Pei, Y.; Zhang, Z.; Luo, J. Study on Frost Resistance Improvement of Foamed Concrete Used as Subgrade Filler. *Constr. Build. Mater.* **2025**, *468*, 140446. [CrossRef]
5. Decký, M.; Drusa, M.; Zgútová, K.; Blaško, M.; Hájek, M.; Scherfel, W. Foam Concrete as New Material in Road Constructions. *Procedia Eng.* **2016**, *161*, 428–433. [CrossRef]
6. Ma, S.; Chen, W.; Zhao, W. Mechanical Properties and Associated Seismic Isolation Effects of Foamed Concrete Layer in Rock Tunnel. *J. Rock Mech. Geotech. Eng.* **2019**, *11*, 159–171. [CrossRef]
7. Zhang, H.; Qi, X.; Wan, L.; Zuo, Z.; Ge, Z.; Wu, J.; Song, X. Properties of Silt-Based Foamed Concrete: A Type of Material for Use in Backfill behind an Abutment. *Constr. Build. Mater.* **2020**, *261*, 119966. [CrossRef]
8. Cai, D.; Wei, S.; Ye, Y.; Zhang, Q.; Li, Z.; Li, S. Mechanical Properties of Lightweight Foam Concrete Filler for Roadbed of High-Speed Railway. *Arab. J. Geosci.* **2021**, *14*, 902–911. [CrossRef]
9. Huang, J.; Cai, D.; Su, Q.; Yao, H.; Fan, R.; Pei, Y.; Zhang, Z.; Yao, J.; Luo, J.; Ou, X. Comparative Study on Static and Dynamic Characteristics of Foamed Concrete Interlayer-Type and Traditional Layered Ballastless Track Subgrades. *Constr. Build. Mater.* **2025**, *470*, 140651. [CrossRef]
10. Zhao, W.; Zhang, K.; Liu, X.; Liu, X. Deformation Monitoring of an Adjacent Subgrade Consisting of Lightweight Foam Concrete in a Loess Region. *Constr. Build. Mater.* **2025**, *458*, 139641. [CrossRef]
11. Hao, Y.; Wang, H.; Qin, L.; Hou, Y.; Shi, Y. Dynamic Characteristics and Response Analysis of a New Type of Prefabricated Fly Ash Foam Concrete Structure. *Structures* **2023**, *57*, 105074. [CrossRef]
12. Su, Y.; Cai, G.; Yin, F.; Shan, Y.; Wang, H. Investigation of the Creep Behavior and Time-Dependent Constitutive Model of Red-Stratum Mudstone Fill Material in High-Fill Subgrade. *Constr. Build. Mater.* **2025**, *458*, 139560. [CrossRef]
13. Liu, D.; Zhang, W.; Tang, Y.; Xie, B.; Shi, Q.; Cao, K. Evolving Support Vector Regression Based on Improved Grey Wolf Optimization for Predicting Settlement during Construction of High-Filled Roadbed. *Transp. Geotech.* **2024**, *45*, 101233. [CrossRef]
14. Zhou, S.; Shan, Y.; Wu, Z.; Zhao, W.; Yang, L.; Lin, Y. Lateral Deformation of High-Speed Railway Foundation Induced by Adjacent Embankment Construction in Soft Soils: Numerical and Field Study. *Transp. Geotech.* **2023**, *41*, 101005. [CrossRef]
15. Wu, Y.; Wu, X.; Zhou, J.; Jia, H.; Yao, Y. Experimental Study on the Dynamic and Static Mechanical Properties of Polyurea-Coated Foam Concrete. *Results Eng.* **2026**, *29*, 109775. [CrossRef]
16. Jiao, Y.; Ang, K.; Su, B.; Qiu, J.; Li, Z.; Yao, X.; Wang, Z.; Shu, X. Static and Dynamic Mechanical Properties of Foamed Concrete under Wide Confinement Level and Strain Rate Ranges. *Constr. Build. Mater.* **2026**, *521*, 146172. [CrossRef]
17. Li, Z.; Chen, W.; Hao, H.; Ha, N.S.; Pham, T.M. Static and Dynamic Properties of Novel Ambient-Cured Lightweight Geopolymer Composites with Fibre Reinforced Epoxy Coated EPS Aggregates. *Compos. Part B* **2023**, *250*, 110439. [CrossRef]
18. Wei, B.; Wei, Y.; Deng, J.; Li, Q.; Huang, S.; Zhu, B. Effects of Modified Bamboo Aggregate on Strength and Microstructure of Ceramsite Concrete. *Constr. Build. Mater.* **2025**, *502*, 144253. [CrossRef]
19. Li, N.; Long, G.; Ma, C.; Fu, Q.; Zeng, X.; Ma, K.; Xie, Y.; Luo, B. Properties of Self-Compacting Concrete (SCC) with Recycled Tire Rubber Aggregate: A Comprehensive Study. *J. Clean. Prod.* **2019**, *236*, 117707. [CrossRef]
20. Shi, X.; Gu, L.; Wang, Z.; Cheng, Z.; Yang, J.; Zhang, G.; Gao, F. Research on Dynamic Mechanical Behaviors and Energy Absorption Characteristics of Ceramsite-Based Foamed Concrete Composite. *Compos. Struct.* **2026**, *383*, 120087. [CrossRef]
21. Wen, S.; Wei, H.; Ma, Z.; Zhang, Y. Experimental Study on Dynamic Characteristics of Saponified Slag Fly Ash Foamed Lightweight Soil. *Soil Dyn. Earthq. Eng.* **2025**, *194*, 109362. [CrossRef]

22. Ma, K.; Ren, F.; Huang, H.; Yang, X.; Zhang, F. Experimental Investigation on the Dynamic Mechanical Properties and Energy Absorption Mechanism of Foam Concrete. *Constr. Build. Mater.* **2022**, *342*, 127927. [CrossRef]
23. Feng, L.; Chen, X.; Ning, Y.; Wang, J.; Zhang, W. High Temperature Effect of Foamed Concrete under Equal Displacement Increment Triaxial Cyclic Compression. *Constr. Build. Mater.* **2022**, *327*, 126989. [CrossRef]
24. Zhang, H.; Liu, M.; Sun, Y.; Yang, Q.; Song, X.; Li, X. Triaxial mechanical characteristic of the silt-based foamed concrete. *J. Shandong Univ. Eng. Sci.* **2022**, *52*, 39–46. [CrossRef]
25. Zhang, H.; Liang, Q.; Sao, M.; Jiang, N.; Yang, M.; Sui, G.; Ge, Z. Influence of circulating refined fluidized bed fly ash on mechanical properties and pore structure of foamed concrete. *Mater. Rep.* **2024**, *38*, 54–60. [CrossRef]
26. Mu, X.; Chen, H.; Chen, X. Experimental Study on Static and Dynamic Properties of Foam Concrete. *J. Yangtze River Sci. Res. Inst.* **2017**, *34*, 126–129. [CrossRef]
27. Mei, L.; Cheng, T.; He, J.; Zhuang, X.; Gu, H. Dynamic Properties of EPS Beads Lightweight Soil Mixed with Polypropylene Fiber. *Case Stud. Constr. Mater.* **2023**, *19*, e02637. [CrossRef]
28. Shi, X.; Huang, J.; Su, Q. Experimental and numerical analyses of lightweight foamed concrete as filler for widening embankment. *Constr. Build. Mater.* **2020**, *250*, 118897. [CrossRef]
29. Wu, J.; Wang, J.; Liu, M.; Zhuang, P.; Zhang, H.; Song, X. Dynamic Properties of Silt-Based Foamed Concrete as Filler in Subgrade. *J. Mater. Civ. Eng.* **2022**, *34*, 04022241. [CrossRef]
30. Li, Z.; Chen, W.; Sun, G.; Chen, Y.; Li, Z.; Li, H.; Hao, H. Dynamic Mechanical Properties of Nanoparticle-Stabilized Foam Concrete (NFC). *Case Stud. Constr. Mater.* **2025**, *22*, e04805. [CrossRef]
31. Gong, J.; Ma, A.; Wang, S.; Zhang, J.; An, Z. Dynamic Mechanical Behavior of Magnesium Oxysulfate-Based Titanogypsum Foamed Concrete: A Macro- and Meso-Scale Investigation. *Case Stud. Constr. Mater.* **2025**, *22*, e04870. [CrossRef]
32. Wang, J.; Xu, Z. Dynamic Mechanical Behaviors of Foamed Concrete Using Modified Viscoelastic SHPB. *J. Build. Eng.* **2024**, *95*, 110185. [CrossRef]
33. Li, M.; Zhang, Y.; Liu, S.; Wu, K.; Wang, Z.; Zhang, X. Dynamic Properties of Alkali Residue-Based Foamed Concrete under Dry-Wet Cycles. *J. Build. Eng.* **2024**, *98*, 111508. [CrossRef]
34. Liu, M.; Liu, Z.; Wang, K.; Ma, C.; Zhang, H.; Zhuang, P. Strength and Deformation Performances of Silt-Based Foamed Concrete under Triaxial Shear Loading. *J. Build. Eng.* **2022**, *60*, 105237. [CrossRef]
35. Ma, Z.; Ma, C.; Du, C.; Zhang, S.; Zhang, H.; Zhang, X.; Zhang, X.; Wang, J.; Tian, M.; Wang, Y. Research on Dynamic Mechanical Properties of Polypropylene Fiber-Modified Rubber Foamed Concrete. *Constr. Build. Mater.* **2023**, *404*, 133282. [CrossRef]
36. Hamada, H.M.; Shi, J.; Abed, F.; Humada, A.M.; Majdi, A. Recycling Solid Waste to Produce Eco-Friendly Foamed Concrete: A Comprehensive Review of Approaches. *J. Environ. Chem. Eng.* **2023**, *11*, 111353. [CrossRef]
37. Zou, Z.; Deng, Z.; Chen, Y.; Hu, J. Strength Prediction of Foam Light Soil Based on GA-BP Neural Network. *J. South China Univ. Technol. Nat. Sci.* **2022**, *50*, 125–132.
38. Zhang, C.; Wang, H.; Wang, B.; Yu, Y.; Zhang, C. Characterization of the porous structure and its influence on mechanical properties of high-content steel slag powder-cement foamed concrete. *Mater. Rep.* **2025**, *39*, 181–189. [CrossRef]
39. Jiang, P.; Chen, Y.; Li, N.; Zhou, L.; Pu, S.; Wang, W. Strength Properties and Microscopic Mechanism of Lime and Fly Ash Modified Expandable Poly Styrene Lightweight Soil Reinforced by Polypropylene Fiber. *Case Stud. Constr. Mater.* **2022**, *17*, e01250. [CrossRef]
40. Bayraktar, O.Y.; Danish, A.; Bodur, B.; Kaplan, G.; Aydın, A.C.; Ozbakkaloglu, T. Performance Assessment of Fiber-Reinforced Coral Aggregate-Based Lightweight Foam Concrete for Sustainable Marine Construction. *Constr. Build. Mater.* **2024**, *449*, 138368. [CrossRef]
41. Ramezani, M.; Vilches, J.; Neitzert, T. Pull-out Behavior of Galvanized Steel Strip in Foam Concrete. *Int. J. Adv. Struct. Eng.* **2013**, *5*, 24–35. [CrossRef]
42. Ye, Y.; Han, J.; Liu, H.; Rachford, S.M.; Parsons, R.L.; Dolton, B.; O'Reilly, M. Pullout Resistance of Geogrid and Steel Reinforcement Embedded in Lightweight Cellular Concrete Backfill. *Geotext. Geomembr.* **2022**, *50*, 432–443. [CrossRef]
43. Li, Y.; Liu, Y.; Zhang, H.; An, N.; Fan, Z. Experimental Study on the Flexural Performance of Geogrid-Reinforced Foamed Lightweight Soil. *Buildings* **2025**, *15*, 461. [CrossRef]
44. Wu, L.; Zhu, Y.; Xu, Q.; Chen, Q.; Wang, Y. Triaxial test study of geogrid reinforced sand. *J. Hefei Univ. Technol. Nat. Sci.* **2024**, *47*, 83–90. [CrossRef]
45. Wang, Z.; Cai, Y.; Qi, Y.; Yang, G.; Ye, Z. Large-scale triaxial tests of geogrid reinforced rubber gravel mixtures. *J. Railw. Sci. Eng.* **2023**, *20*, 2509–2520. [CrossRef]
46. Yao, Y. Study on Structure Optimization and Dynamical Response of Semi-Rigid Pavement Based on Foamed Lightweight Soil Composite Subgrade. Master's Thesis, Shandong University, Jinan, China, 2021. [CrossRef]
47. Li, M.; Zhang, Y.; Liu, S.; He, H.; Wang, Z.; Zhang, X. Dynamic Properties of Alkali Residue-Based Foamed Concrete under Cyclic Load. *Constr. Build. Mater.* **2024**, *438*, 137060. [CrossRef]

48. Chang, J.; Li, X.; Zhang, F.; Liang, S.; Feng, H. Degradation mechanism of railway ballast by large-scale cyclic triaxial test and image analysis method. *J. China Railw. Soc.* **2022**, *44*, 107–116. [CrossRef]
49. Du, X.; Zhu, L.; Li, Y.; Wang, H.; Xu, K. Research on the Damage Evolution Law of Iron Tailing Sand Based Foam Concrete under Cyclic Loading. *Case Stud. Constr. Mater.* **2024**, *21*, e04117. [CrossRef]
50. Dong, Z.; Zhai, P.; Zeng, F.; Li, J.; Zhang, Q. Experimental study on dynamic shear modulus and damping ratio of silty soil in the yellow river flooded area. *J. Henan Univ. Ed. Nat. Sci.* **2020**, *50*, 332–340. [CrossRef]
51. Ma, X.; Liang, Q.; Zhao, T.; Zhou, W. Review and further consideration on research of soil dynamics. *World Earthq. Eng.* **2021**, *37*, 217–230.
52. Peng, F.; Li, M.; Li, Y.; Huang, M. Dynamic Modulus and Damping Ratio Characteristics of Unsaturated Silt in the Yellow River Flood Field. *J. Cent. South Univ.* **2024**, *31*, 237–249. [CrossRef]
53. Tang, F.; Zhang, W.; Tang, X.; Liu, C. Study on the dynamic characteristics of geogrid reinforced loess under cyclic loading. *Water Resour. Hydropower Eng.* **2024**, *55*, 148–161. [CrossRef]
54. Xu, T.; He, Z.; Wen, H. Study on the dyamic properties and applicability of the dynamic constitutive model of silt in yellow river flood area. *J. Henan Univ. Ed. Nat. Sci.* **2019**, *49*, 369–378. [CrossRef]
55. Tao, H.; Zheng, W.; Zhou, X.; Zhou, L.; Li, C.; Yu, Y.; Jiang, P. Study on Dynamic Modulus and Damping Characteristics of Modified Expanded Polystyrene Lightweight Soil under Cyclic Load. *Polymers* **2023**, *15*, 1865. [CrossRef] [PubMed]
56. Rasa, A.Y.; Budak, A. Soil-Structure-Trench Interaction Effects on Vibration Isolation of Multi-Story Structures. *J. Braz. Soc. Mech. Sci. Eng.* **2026**, *48*, 186. [CrossRef]

Disclaimer/Publisher's Note: The statements, opinions and data contained in all publications are solely those of the individual author(s) and contributor(s) and not of MDPI and/or the editor(s). MDPI and/or the editor(s) disclaim responsibility for any injury to people or property resulting from any ideas, methods, instructions or products referred to in the content.